PCCP

PAPER

View Article Online
View Journal | View Issue

Cite this: *Phys. Chem. Chem. Phys.*, 2018, **20**, 18097

Multi-step phase-cycling in a free-electron laser-powered pulsed electron paramagnetic resonance spectrometer†

C. Blake Wilson, [ab] Samuel Aronson,[a] Jessica A. Clayton,[ab] Steffen J. Glaser, [c] Songi Han [bd] and Mark S. Sherwin *[ab]

Received 22nd March 2018,
Accepted 6th June 2018

DOI: 10.1039/c8cp01876f

rsc.li/pccp

Electron paramagnetic resonance (EPR) is a powerful tool for research in chemistry, biology, physics and materials science, which can benefit significantly from moving to frequencies above 100 GHz. In pulsed EPR spectrometers driven by powerful sub-THz oscillators, such as the free electron laser (FEL)-powered EPR spectrometer at UCSB, control of the duration, power and relative phases of the pulses in a sequence must be performed at the frequency and power level of the oscillator. Here we report on the implementation of an all-quasioptical four-step phase cycling procedure carried out directly at the kW power level of the 240 GHz pulses used in the FEL-powered EPR spectrometer. Phase shifts are introduced by modifying the optical path length of a 240 GHz pulse with precision-machined dielectric plates in a procedure we call phase cycling with optomechanical phase shifters (POPS), while numerical receiver phase cycling is implemented in post-processing. The POPS scheme was successfully used to reduce experimental dead times, enabling pulsed EPR of fast-relaxing spin systems such as gadolinium complexes at temperatures above 190 K. Coherence transfer pathway selection with POPS was used to perform spin echo relaxation experiments to measure the phase memory time of P1 centers in diamond in the presence of a strong unwanted FID signal in the background. The large excitation bandwidth of FEL-EPR, together with phase cycling, enabled the quantitative measurement of instantaneous electron spectral diffusion, from which the P1 center concentration was estimated to within 10%. Finally, phase cycling enabled saturation-recovery measurements of T_1 in a trityl-water solution at room temperature – the first FEL-EPR measurement of electron T_1.

1 Introduction

Pulsed electron paramagnetic resonance (EPR) is an established technique with broad applications in physics, material science, chemistry, and biochemistry.[1–3] Extending pulsed EPR to higher fields and frequencies provides several advantages, including but not limited to increased intrinsic sensitivity, time resolution, and spectral resolution. These advantages are especially useful for studying, for example, biological samples[4–6] in which high resolution is required, but where sample volumes are limited, for performing precision measurements of electron *g*-tensors,[5,7,8] and for high-resolution measurements of impurity centers in a variety of solid-state systems, such as substitutional nitrogen (P1) and nitrogen-vacancy (NV) centers in diamond.[9–11] Pulsed dipolar spectroscopy techniques[12,13] conducted at high field can provide orientation selectivity,[14–16] or can take advantage of favorable high-field spectral properties of high-spin, half-integer metal centers.[17–22] Additionally, relaxation time measurements performed at high field can yield important information about spin–spin coupling and decoherence,[9] and about spin clustering.[23]

Unfortunately, many of the principal advantages of high-field pulsed EPR are difficult to realize in practice, given the lack of techniques for generating high-power, high-frequency microwave and THz radiation, especially above ~100 GHz. Pulsed EPR spectrometers powered by frequency-multiplied microwave sources are available commercially at 263 GHz with tens

[a] *Department of Physics, University of California, Santa Barbara, Santa Barbara, California, USA. E-mail: sherwin@physics.ucsb.edu*
[b] *Institute for Terahertz Science and Technology, University of California, Santa Barbara, Santa Barbara, California, USA*
[c] *Department of Chemistry, Technical University of Munich, Garching, Germany*
[d] *Department of Chemistry and Biochemistry, University of California, Santa Barbara, Santa Barbara, California, USA*

† Electronic supplementary information (ESI) available: Additional experimental details provided, including time-domain signals from two-pulse experiments performed on diamond P1 centers, and the particular phase cycling scheme employed. Further, details of how optimal numerical phase shifts were selected for coherence transfer pathway selection are presented, as well as calculations of optical path length differences and THz beam offsets produced by dielectric phase shifter plates. See DOI: 10.1039/c8cp01876f

of mW of power, and at similar frequencies in a few specialized labs.[11,24–30] Spectrometers operating around 95 GHz powered by ~kW extended interaction Klystron (EIK) amplifiers have been more widely employed.[31–33] Recently developed gyrotron-amplifiers[34,35] show promise as potential candidates for integration into magnetic resonance spectrometers. However, above ~100 GHz EIK amplifiers and other vacuum electronic amplifiers yield lower power, and their implementation in magnetic resonance is rare. Operation with tens of mW necessitates either the use of pulses longer than 100 ns, which result in narrow excitation bandwidths relative to the ~10 MHz to ~GHz linewidths common in high-field EPR experiments, or the use of microwave cavities, which dramatically restrict the allowed sample volume, as well as the excitation and detection bandwidth. In both scenarios, the promised improvements in sensitivity at high-fields is impeded. For example, at 240 GHz typical nitroxide radical lineshapes are more than 1 GHz broad. At 140 GHz and above, sample volumes used with high-Q resonators are limited to less than ~250 nL,[28] and excitation bandwidths are limited to a few hundred MHz. In addition, many samples, particularly aqueous samples of interest in studies of biological systems, are extremely lossy at high frequencies.

Gyrotrons and free electron lasers (FELs) are oscillators that can generate powers in excess of 1 kW in the sub-THz frequency range.[36–39] Gyrotrons producing 5–20 W of power have been used in dynamic nuclear polarization (DNP) enhanced NMR experiments,[40,41] and recently a frequency-agile gyrotron[42] was employed to achieve DNP with electron spin decoupling.[43] An EPR spectrometer operating at 240 GHz[44] using the UCSB mm-wave FEL as a source has been developed, operating at power levels of ~500 W to 9 kW, and capable of applying 12 ns inversion pulses to spin-1/2 systems without using a cavity. The UCSB FEL delivers one 3 to 5 μs long pulse, once every second (hereafter, we call this a ''long pulse'' or a ''long FEL pulse''), from which sequences of either one or two ''short pulses'' are ''sliced'' using light-activated semiconductor switches.[45] The amplitude, duration, and temporal separation of each sliced pulse can be independently controlled. Laser-activated switches have also been used to ''slice'' pulses from the output of a gyrotron.[46] FEL-EPR has so far enabled measurement of free-induction decays, Hahn-echoes, and phase memory times as short as 60 ns. However, controlling the relative phase of these two FEL-derived pulses has not been possible to date.

In order to take full advantage of a sequence of pulses in an EPR experiment, it is necessary to control the relative phase of the pulses in a process called phase cycling.[47–49] Phase cycling is standard in pulsed NMR and most pulsed EPR experiments, and is typically achieved using electronic phase shifters. Electronic phase shifters become increasingly difficult to implement, however, as frequencies rise above 100 GHz. High-frequency EPR experiments based on amplifier-multiplier chains (AMCs) have overcome this challenge by implementing appropriate phase control at low frequencies, before frequency multiplication. In recent years, much progress has been made developing EPR spectrometers with arbitrary waveform generators capable of rapid phase (and amplitude) modulation,[50] including at high frequencies in an AMC-based spectrometer.[51]

This approach is not possible in a pulsed EPR experiment based on a high-power sub-THz or THz oscillator. In the case of the UCSB FEL-powered EPR spectrometer, phase control must be implemented directly in the few-kW 240 GHz beam. Briefly, while the frequency of each long FEL pulse is controlled by injection-locking,[52] the phase is not controlled, and so varies from long FEL pulse to long FEL pulse. Previous work[53] has shown that despite the fact that each long FEL pulse has a random phase, coherent signal averaging is still possible. By digitizing the residual of the (heavily attenuated) FEL pulse along with the EPR signal for each experiment and storing all digitized experimental signals (transients), the phase of each transient can be phase-corrected in post processing (after the experiments are completed). In addition, it has been shown that the phase difference between two short pulses sliced from the same long FEL pulse could be reliably controlled by inserting dielectrics into the beam path of one of the two pulses.[53]

In this manuscript, we expand upon the work of Edwards *et al.*[53] by showing that precision-machined dielectrics can be used to accurately control the relative phase between two short pulses traveling down separate optical paths. A set of eight high density polyethylene (HDPE) plates machined to ~10 μm precision in thickness were used in pairs to vary the relative optical path lengths of two ''sliced'' pulses, a procedure we refer to as phase cycling with optomechanical phase shifters (POPS).

Phase determination and correction for each experiment is accomplished in post-processing. We show that by selecting the appropriate set of post-processed numerical receiver phases, different coherence transfer pathways can be selected from the same dataset, making POPS a form of multiplexed phase cycling scheme.[54] We employ POPS to perform two-pulse FEL-EPR experiments at 240 GHz that would otherwise be impossible. We show that two-step POPS can reduce the experimental dead time in two-pulse Hahn echo experiments, allowing for phase memory time measurements of frozen solutions of $GdCl_3$ at temperatures as high as 192 K. We demonstrate that the overlapping signal from a free induction decay (FID) and a two-pulse echo generated from P1 centers in type 1b diamond can be separated, enabling accurate measurements of T_2 and quantification of instantaneous spectral diffusion. We further demonstrate phase-cycled saturation-recovery experiments to measure T_1 of a narrow-line trityl radical at room temperature in an aqueous solution – the first T_1 measurement made using FEL-EPR. The POPS method should be applicable to quasi-optical pulsed EPR spectrometers based on, but not limited to, free-running, phase stable, sources such as FELs and gyrotrons.[46]

2 Phase cycling with optomechanical phase shifters

2.1 Theory

The ability to select a desired coherence transfer pathway makes it possible to separate signals based on different coherence order, p, visited during the course of the experiment.[47,55]

For an uncoupled spin 1/2, the operators $S^+ = S_x + iS_y$, S_z, and $S^- = S_x - iS_y$ have coherence order +1, 0, and −1, respectively. At thermal equilibrium, the traceless part of the density operator is proportional to S_z, *i.e.* magnetic resonance experiments typically start with coherence order $p = 0$. Depending on its flip angle, a pulse may (fully or partially) change the coherence order. During a delay between pulses, the coherence order is constant (neglecting relaxation). In quadrature detection, only density operator components proportional to S^- can lead to observable signals, and hence only coherence order pathways that end at coherence order $p = -1$ need to be considered. A given pulse sequence can provide different information about a spin system depending on the selected coherence transfer pathway. The pulse sequences are designed to select a desired coherence order pathway by cycling the pulse phase and/or by using pulsed magnetic field gradients.[56–58] In the context of the FEL experiments considered here, we focus on phase cycling for coherence pathway selection.

In standard phase cycling schemes, the phases of pulses and of the receiver are systematically varied as an experiment is repeated. Based on a discrete Fourier analysis, it is straightforward to design phase cycles to achieve a desired coherence order change Δp with an individual pulse.[56–58] When multiple pulses are involved, individual phase cycles for each of the pulses can be nested. However, in a sequence consisting of two pulses, only the relative phase of the two pulses is important. Without loss of generality, we assume in the following that only the phase of the first pulse is systematically varied in a phase cycle, while the phase of the second pulse is fixed. Starting from thermal equilibrium with $p = 0$, only coherence order changes Δp of +1, 0, and −1 need to be considered. During a pulse with phase φ which changes the coherence order by Δp, the phase of the signal corresponding to that pathway changes by $-\Delta p\varphi$. The minimum-length phase cycles have three steps with pulse phases of 0°, 120°, and 240°. Here, we consider a (slightly redundant) four-step phase cycle with pulse phases of 0°, 90°, 180°, and 270°. A change of coherence order during the first pulse of $\Delta p = 1$ selects the coherence transfer pathway corresponding to a Hahn echo for the measurement of T_2. A change of coherence order of $\Delta p = 0$ selects the free induction decay (FID) generated by the second pulse and allows one to measure T_1. A change of coherence order of $\Delta p = -1$ would select the FID generated by the first pulse, which is in general undesirable in a two-pulse experiment. The coherent transfer pathways we considered are outlined in Fig. 1.

Phase cycling schemes are accomplished in FEL-EPR at 240 GHz by varying the relative optical path lengths of two short pulses. Fig. 2 shows a schematic of the FEL-EPR pulse slicer used to generate two short pulses of variable duration from a single long FEL pulse. Phase shifts were engineered by selectively varying the optical path length (OPL) of the first pulse with precision-machined high density polyethylene (HDPE) plates, shown in Fig. 2. HDPE was chosen for its favorable optical and mechanical properties, as it is transparent to 240 GHz radiation[59,60] and can be machined to precise tolerances. A plate with index of refraction n and thickness h causes a change

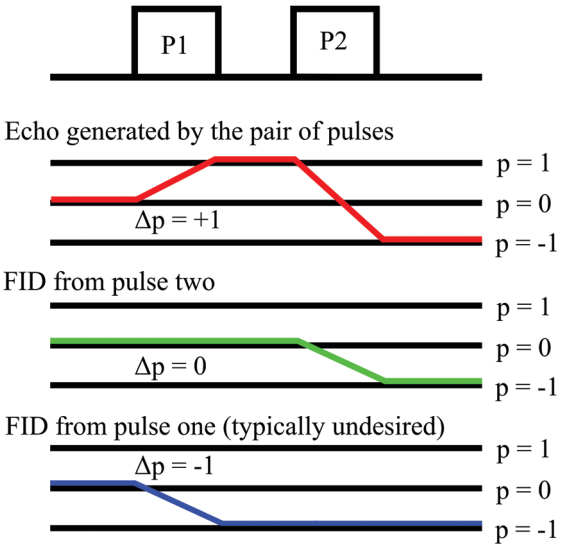

Fig. 1 Three coherence transfer pathways generate observable signal in a standard two-pulse EPR experiment. The top path and the middle path trace the coherences corresponding to the two-pulse echo and the FID generated by the second pulse, respectively. The bottom path traces the coherence corresponding to the FID generated by the first pulse, and is not desired in a standard two-pulse experiment. The coherence order change during pulse one is different for the three paths. This allows for phase cycling to be used to separate each of the three coherence pathways.

in the optical path length $\Delta\mathrm{OPL}(n,h,\theta)$, when inserted into a THz beam at angle of incidence Θ_I, given by

$$\Delta\mathrm{OPL} = h\left(n\sqrt{1-\frac{\sin^2\Theta_\mathrm{I}}{n^2}} - \cos\Theta_\mathrm{I}\right) \quad (1)$$

This in turn produces a phase shift $\Delta\varphi = 2\pi\Delta\mathrm{OPL}/\lambda_0$, where λ_0 is the wavelength of the THz beam in air.

2.2 POPS procedure

HDPE plates were employed in pairs in order to minimize beam offset (see ESI†), with each plate contributing $\Delta\varphi/2$. The plate thicknesses h were chosen to generate total relative phase shifts, $\Delta\varphi$, of 0°, 90°, 180°, and 270°, satisfying

$$\frac{\Delta\mathrm{OPL}}{\lambda_0} = \frac{1}{2}(a+m) \quad (2)$$

at Brewster's angle, where m is a positive integer and a is given in Table 1, so that

$$h = \frac{1}{2}\frac{\sqrt{1+n^2}}{n^2-1}(a+m)\lambda_0 \quad (3)$$

The plate thicknesses were chosen to be as thin as possible while satisfying eqn (3), and while remaining thick enough to avoid warping during machining.

Phase cycling with optomechanical phase shifters (POPS) was carried out in several steps, which are outlined here.

Step 1: Stochastic phase cycling and coherent signal averaging. Fig. 2 illustrates schematically a two-pulse FEL-EPR experiment.

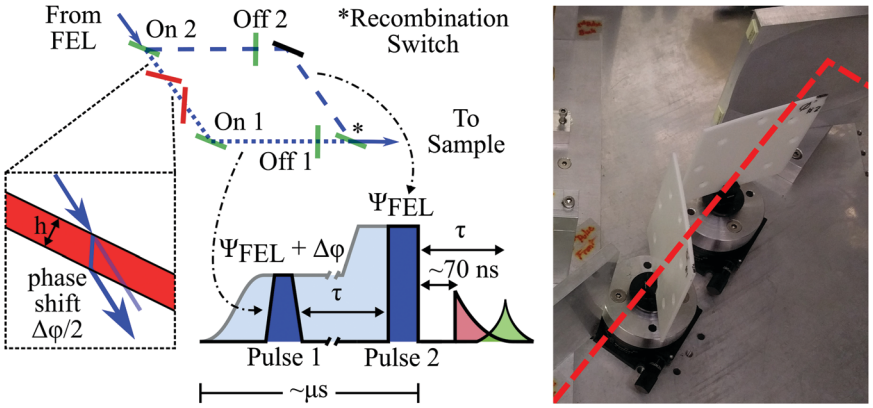

Fig. 2 Schematic illustrating the pulse slicer used in a typical two-pulse FEL-EPR experiment. Optically activated silicon switches are used to slice two short pulses out of the FEL pulse, which travel down two spatially separated optical paths and which are recombined before being sent to the sample. Two silicon switches function as "on" switches, which re-direct the 240 GHz beam into the sample path, while another two switches function as "off" switches, terminating each short pulse. The recombination switch turns on simultaneously with the second "on" switch ("On 2"), and allows for the two beams to be recombined into the same final path to the sample. Dielectric phase shifter plates inserted into the path of the first pulse increment the phase difference $\Delta\varphi$ between the two pulses. Phase shifter plates operate at the Brewster angle in pairs, to minimize beam offset, with each plate inducing a phase shift of $\Delta\varphi/2$. Also shown is a time-domain schematic of a two-pulse FEL-EPR experiment, showing the FEL pulse (light blue), the two pulses sliced from the longer FEL pulse (dark blue), and the signals generated by the pair of pulses: a FID (red) and an echo (light green), which often overlap in time. Below is a photo of a pair of phase shifter plates inserted into the optical path of the first pulse.

Table 1 Thicknesses of each HDPE phase-shifter plate machined for use in POPS experiments. The phase shift produced by each plate is half of the shift quoted in the left hand column, as plates are designed to work in pairs

Desired total $\Delta\varphi$ (°)	a	m	Thickness (mm)
0	0	3	2.60 ± 0.01
90	1/4	2	1.95 ± 0.01
180	1/2	2	2.17 ± 0.01
270	3/4	2	2.39 ± 0.01

POPS is applied in batches, so that a series of transients is acquired at a given inter-pulse phase difference $\Delta\varphi$. The FEL phase Ψ_{FEL} is random from FEL pulse to FEL pulse, but is stable during a given FEL pulse. Phase-sensitive signal averaging is implemented using a procedure described by Edwards *et al.*[53] Briefly, the method leverages the fact that heavily attenuated residual light from the FEL reaches the detector and is digitized prior to the acquisition of the EPR signal. The random FEL phase Ψ_{FEL} is determined from the residual light, and is used to phase-correct each transient in post-processing. These transients are then coherently added for a particular $\Delta\varphi$ achieved by POPS to produce a complex signal $S(t)$. This approach to coherent signal averaging is comparable to the CYCLOPS (CYClical Ordered Phase Sequence)[61] in the limit of many pulses.[53] In a two-pulse experiment as implemented here, the residual light from the second pulse is used to determine Ψ_{FEL}.

Step 2: Modify the relative phase between the two pulses. After completing the experiment with a fixed phase difference $\Delta\varphi_0$ between pulses one and two, producing a complex signal $S_0(t)$, the phase difference $\Delta\varphi_i$ is modified by inserting dielectric phase shifter plates into the optical path of the first pulse. After this has been accomplished, a second batch of transients, $S_1(t)$, with a fixed $\Delta\varphi_1$ is coherently averaged.

Sampling all desired inter-pulse phase differences, a set of averaged complex signals, $\{S_i(t)\}$, is acquired, with one averaged signal for each $\Delta\varphi_1$ sampled. Each signal of this set is stored separately for further processing. The "global" phase for this data set is determined by choosing one averaged signal $S_0(t)$ to act as a reference, and adjusting the phase of the other averaged signals $S_i(t)$ relative to the reference in the same manner as outlined above, again using the residual FEL light from the second pulse.

Step 3: Measure the applied phase shifts. In practice, the set of experimentally determined phase shifts $\{\Delta\varphi_i\}$ were found to differ, sometimes by several degrees, from experiment to experiment, likely due to the difficulty of reproducibly inserting the phase shifter plates into the pulse slicer with sufficient precision. It was therefore necessary to measure each phase $\Delta\varphi_i$ for each experiment, using the same method of post-processing phase correction as was used in steps 1 and 2. Here, the residual light from the first pulse was used to experimentally determine the set of phase differences $\{\Delta\varphi_i\}$ induced by POPS.

Step 4: Apply numerical phase shifts in post-processing. An additional set of numerical receiver phase shifts $\{\theta_i\}$ is finally applied to the recorded signals $\{S_i(t)\}$, in order to perform coherence transfer pathway selection in a multiplexed fashion.[54] The N recorded signals are then added together to generate the final output signal $S(t)$

$$S(t) = \frac{1}{N}\sum_i S_i(t)\exp(-i\theta_i) \quad (4)$$

The final output signal of a two-pulse POPS experiment, where the phase of the second pulse is held constant, contains contributions from each coherence transfer pathway Δp weighted by the complex coefficients $P(\{\Delta\varphi_i\},\{\theta_i\},\Delta p)$[54]

$$P(\{\Delta\varphi_i\},\{\theta_i\},\Delta p) = \frac{1}{N}\sum_i \exp(-i(\Delta p\Delta\varphi_i + \theta_i)) \quad (5)$$

Numerical phase shifts $\{\theta_i\}$ are chosen so that

$$P(\{\Delta\varphi_i\},\{\theta_i\},\Delta p) = \begin{cases} 1 & \text{Desired } \Delta p \\ 0 & \text{Undesired } \Delta p \end{cases} \quad (6)$$

As an example, if the phase of the first pulse is cycled through $\{\Delta\varphi_i\} = \{0,\pi/2,\pi,3\pi/2\}$, then any of the three pathways shown in Fig. 1 can be selected by choosing appropriate sets of numerical receiver phase shifts. With the phase of the second pulse held effectively constant, the three coherence transfer pathways each pick up difference phases given by $\{-\Delta p\Delta\varphi_i\}$. In this example, the $\Delta p = +1$ pathway, corresponding to the echo, concludes the two-pulse experiment with a phase which is stepped through $\{0,-\pi/2,\pi,-3\pi/2\} = \{0,3\pi/2,\pi,\pi/2\}$. Therefore, the echo can be selected by cycling the numerical receiver phase through $\{\theta_i\} = \{0,3\pi/2,\pi,\pi/2\}$, so that $P(\{\Delta\varphi_i\},\{\theta_i\},\Delta p = +1) = 1$. At the same time, the phase of the $\Delta p = 0$ pathway, corresponding to the FID from the second pulse, is not changed as $\Delta\varphi$ is cycled, while the phase of the $\Delta p = -1$ pathway, corresponding to the FID from the first pulse, is stepped through $\{0,\pi/2,\pi,3\pi/2\}$, so that $P(\{\Delta\varphi_i\},\{\theta_i\},\Delta p = 0) = P(\{\Delta\varphi_i\},\{\theta_i\},\Delta p = -1) = 0$. Therefore, the choice of the numerical receiver phase shifts $\{\theta_i\} = \{0,3\pi/2,\pi,\pi/2\}$ selects the echo and suppresses the other two coherences. However, by instead choosing $\{\theta_i'\} = \{0,0,0,0\}$, the same set of signals $\{S_i(t)\}$ can be used to select the FID from the second pulse, since $P(\{\Delta\varphi_i\},\{\theta_i'\},\Delta p = 0) = 1$ and $P(\{\Delta\varphi_i\},\{\theta_i'\},\Delta p = \pm 1) = 0$. Finally, by choosing $\{\theta_i''\} = \{0,\pi/2,\pi,3\pi/2\}$, the same set of signals $\{S_i(t)\}$ can be used to select the $\Delta p = -1$ pathway, corresponding to the FID from the first pulse, as $P(\{\Delta\varphi_i\},\{\theta_i''\},\Delta p = -1) = 1$ in this case and $P(\{\Delta\varphi_i\},\{\theta_i''\},\Delta p = +1) = P(\{\Delta\varphi_i\},\{\theta_i''\},\Delta p = 0) = 0$.

2.3 Correcting for non-ideal pulse phases

There are many sets of pulse phase shifts $\{\Delta\varphi_i\}$ and numerical receiver phase shifts $\{\theta_i\}$ that can be used to select a particular coherence transfer pathway. For the example illustrated previously, where $\{\Delta\varphi_i\} = \{0,\pi/2,\pi,3\pi/2\}$, it was possible to select any of the three coherence transfer pathways by finding sets of $\{\theta_i\}$ for which eqn (6) is exactly satisfied. However, when the phase of the first pulse is cycled through an arbitrary set of angles $\{\Delta\varphi_i\} = \{\Delta\varphi_0,\Delta\varphi_1,\Delta\varphi_2,\Delta\varphi_3\}$, selecting the correct set of numerical receiver phases $\{\theta_i\}$ to select a particular coherence transfer pathway is not straightforward. Following the previous example, when the applied phase shifts $\{\Delta\varphi_i\}$ deviate from $\{0,\pi/2,\pi,3\pi/2\}$, it is necessary to choose new and different sets of numerical phase shifts $\{\theta_i\}$ for the receiver phase to correctly select each of the three Δp pathways. In general, for an arbitrary set of phase shifts $\{\Delta\varphi_i\}$, eqn (6) cannot be exactly satisfied. The optimal choice of numerical receiver phases should both maximally attenuate unwanted coherences and maximally preserve desired coherences. Note that this situation is different from the scenario typically encountered in magnetic resonance experiments, where the optimal choices of pulse and receiver phases are made together.

Two procedures were developed to estimate the optimal numerical phase shifts $\{\theta_i\}$ in a four-step POPS phase cycle, given a set of phases $\{\Delta\varphi_i\}$. The "least squares method" relies on least-squares minimization to assign the approximately correct receiver phases $\{\theta_i\}$ to minimize unwanted coherences. The "echo-optimized method" was designed specifically to isolate the echo pathway ($\Delta p = +1$, see Fig. 1), and does not involve any minimization routine. The echo-optimized method has the advantage of always guaranteeing complete cancellation of unwanted coherences, and can in addition be modified to select for the $\Delta p = -1$ coherence pathway. The least-squares method is by contrast more flexible, as it can be used to select for $\Delta p = 0$.

The least-squares method was based on varying the receiver phases $\{\theta_i\}$ to both minimize signals from unwanted coherences, and to correctly set the phase of the desired coherence. To accomplish this, eqn (6) was solved for the four values of the receiver phase $\{\theta_i\}$ in a least-squares sense. When trying to select one Δp, the real and imaginary parts of eqn (6) together provide six equations from which to extract the four unknown phases $\{\theta_i\}$. This method can be modified by assigning weights to the quantities $P(\{\Delta\varphi_i\},\{\theta_i\},\Delta p)$ in eqn (6), in order to determine receiver phase shifts which penalize one unwanted coherence pathway over another. This is desirable in cases where, for example, there is no signal in the detection window corresponding to the FID from the first pulse (the $\Delta p = -1$ pathway). The least-squares method can be used to select any of the three coherence transfer pathways corresponding to Δp.

The echo-optimized method, by contrast, uses a combination of receiver phase shifts and selective signal scaling to completely remove contributions from the $\Delta p = -1$ and the $\Delta p = 0$ coherence transfer pathways (corresponding to the FIDs from the first and second pulses, respectively), leaving only the contributions from the $\Delta p = +1$ pathway (corresponding to the echo). The echo-optimized method consists of two steps.

Step 1. Two signals $F_1(t)$ and $F_2(t)$ are created from the set of four complex signals $\{S_0(t),S_1(t),S_2(t),S_3(t)\}$ by adding the four signals with individual phase shifts as follows,

$$F_1(t) = \frac{1}{2}(S_0(t) + S_1(t) - S_2(t) - S_3(t)) \quad (7a)$$

$$F_2(t) = \frac{1}{2}(S_0(t) - S_1(t) - S_2(t) + S_3(t)) \quad (7b)$$

Because the $\Delta p = 0$ pathway does not change sign as the phase of the first pulse is varied, the difference of two signals $S_i(t) - S_j(t)$ does not contain any signal corresponding to this pathway. Therefore, by construction, these two signals only include contributions from the $\Delta p = \pm 1$ pathways.

Step 2. Contributions from the $\Delta p = -1$ pathway are eliminated by taking a linear combination of $F_1(t)$ and $F_2(t)$, yielding the complex echo signal $E_{+1}(t)$,

$$E_{+1}(t) = c_1F_1(t) + c_2F_2(t) \quad (8)$$

The complex coefficients c_1 and c_2 can be calculated by tracking the evolution of $P(\{\Delta\varphi_i\},\{\theta_i\},\Delta p)$ (eqn (6)) through the phase shifts applied in eqn (7), given by the two complex numbers

$$v_1 = e^{-i\varphi_0} + e^{-i\varphi_1} - e^{-i\varphi_2} - e^{-i\varphi_3} \quad (9a)$$

$$v_2 = e^{-i\varphi_0} - e^{-i\varphi_1} - e^{-i\varphi_2} + e^{-i\varphi_3} \quad (9b)$$

so that $c_1 = iv_1/|v_1|^2$ and $c_2 = -iv_2/|v_2|^2$. For the case where $\{\varphi_i\} = \{0,\pi/2,\pi,3\pi/2\}$, this method reproduces the expected result $E_{+1}(t) = (S_0 + S_1e^{-i3\pi/2} + S_2e^{-i\pi} + S_3e^{-i\pi/2})/4$.

3 Spin relaxation time measurements using FEL-EPR and POPS

3.1 High temperature phase memory time measurements of Gd^{3+} ions with two-step POPS

Gadolinium complexes are often used as spin labels[62] for distance measurements using pulsed dipolar spectroscopy techniques,[63] lineshape measurements,[64,65] or other experimental schemes, such as relaxation-induced dipolar modulation (RIDME)[66] spectroscopy. Therefore, high-field measurements of gadolinium phase memory times at or near physiological temperatures are extremely important. T_m for gadolinium complexes in frozen glassy matrices decreases strongly with increasing temperature and field,[67] making it impossible to perform Hahn echo experiments above ~100 K at 240 GHz with a 50 mW solid-state microwave source and our current non-resonant probe design. Two-step POPS was used to reduce the experimental dead time in electron spin echo decay experiments performed on frozen glassy solutions of $GdCl_3$ containing Gd^{3+} ions as shown in Fig. 3. Reducing the dead time makes it possible to measure shorter phase memory times T_m, and improves the accuracy of T_m measurements.

In FEL-EPR Hahn echo experiments without phase cycling, detection artifacts caused by standing waves and scattered light produced by the second pulse partially obscure the desired EPR signal, limiting the experimental dead time to ~70 ns. These artifacts appear in Fig. 3a as distortions in the beginning of the echo signal. These artifacts are effectively eliminated by a two-step phase cycle, as shown in Fig. 3b. When the Hahn echo experiment is repeated with the phase of the first pulse inverted but the phase of the second pulse held constant, the phase of the echo also inverts. However, the phase of artifacts due to scattered light and standing waves produced by the second pulse does not change. By subtracting the complex signal

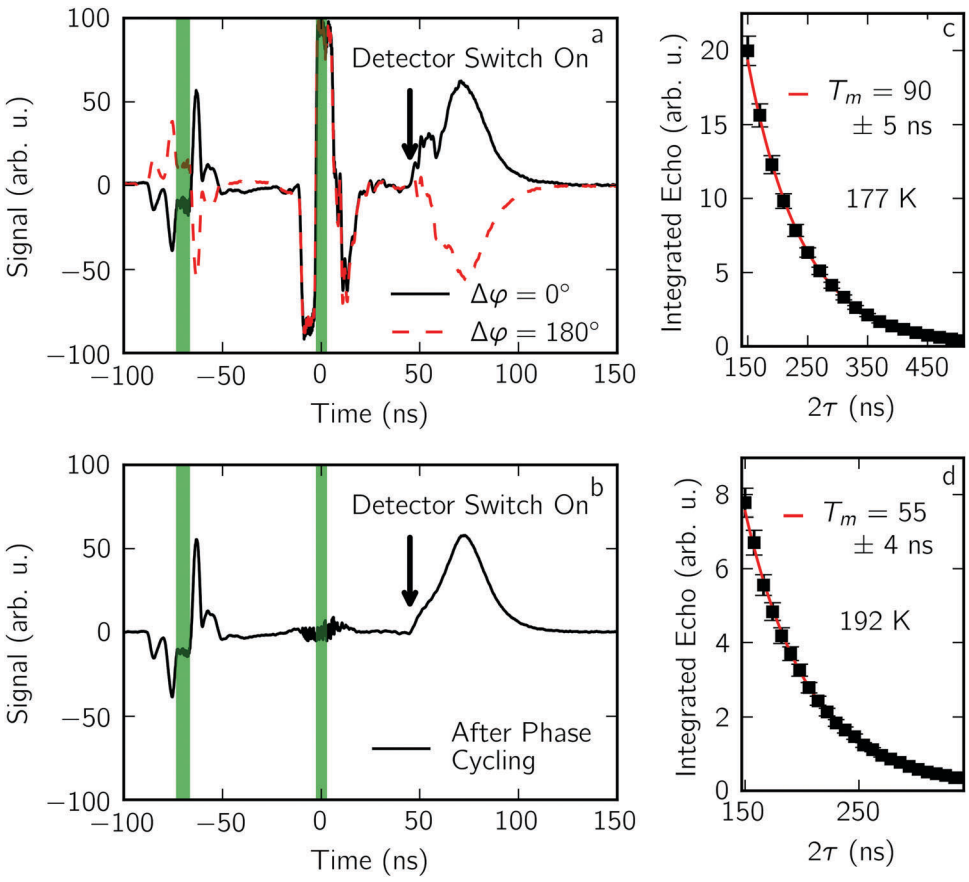

Fig. 3 (a) Time domain signal from a two-pulse FEL-EPR experiment, performed on 1 mM $GdCl_3$ in a 0.6 : 0.4 v : v solution of glycerol-d_8 : D_2O at 177 K. The pulse lengths were 11 ns for pulse one and 7 ns for pulse two, with the pulse positions shown in green. A silicon protection switch is activated by a pulse of 530 nm light from a Nd:YAG laser 50 ns after the second pulse, when there is still appreciable scattered light reaching the detector. Signal recorded before this is due to incomplete detector isolation, which is exploited to enable phase sensitive detection. The solid black trace shows real channel signal when no phase shifter plates are inserted, and the red dashed trace shows the real channel signal when the phase of the first pulse is shifted by 180°. The initial echo is distorted by scattered light reaching the detector. Both signals are demodulated from the 500 MHz digitization frequency. (b) The real channel signal after two-step POPS, showing much reduced echo distortion and cancellation of the leaked light from the second pulse. Two-step POPS was used to perform phase memory time measurements at (c) 177 K and (d) 192 K, with the pulse lengths described above.

generated by the second experiment from the complex signal generated by the first experiment, such detection artifacts are largely eliminated, allowing for nearly artifact-free data acquisition to begin ~50 ns after the end of the second pulse, representing an improvement of the dead time before detection by ~20 ns. With POPS-assisted FEL-EPR, the phase memory time T_m was measured for 1 mM $GdCl_3$ in a frozen glassy solution to be 90 ± 5 ns at 177 K (Fig. 3c), and 55 ± 4 ns at 192 K (Fig. 3d).

The reduced experimental dead time in two pulse echo experiments allows for the use of shorter inter-pulse delays. The shortest useful inter-pulse delay is limited by the minimum experimental dead time, but is also somewhat experiment-dependent. When the experiment involves integrating the entire echo, as is the case in the T_m measurements reported in Fig. 3c and d, then the shortest useful inter-pulse delay must be long enough that the entire echo occurs after the minimum experimental dead time. If, however, only the peak of the echo is required for an experiment, then the shortest useful inter-pulse delay can be made as short as the minimum experimental deadtime.

3.2 Measurements of phase memory time and instantaneous spectral diffusion in diamond P1 centers

P1 centers in diamond are substitutional nitrogen defects, which in type 1b diamond are typically present at about 10–100 parts per million (ppm).[11] P1 center concentration and spatial configuration have been shown to play a dominant role in the decoherence rate, $1/T_2$, of both P1 centers and nitrogen-vacancy (NV) centers in type 1b diamond.[68,69] Precisely determining the concentration of P1 centers in diamond is therefore of great interest, especially in light of recent efforts to fabricate NV center ensembles for NV-based quantum devices.[70–72] Recently, double electron–electron resonance (DEER) measurements at 115 GHz have been used to quantify P1 center concentration.[11] Instantaneous spectral diffusion provides another method for quantifying P1 center concentration. Two-pulse FEL-EPR experiments were performed on P1 centers in type 1b diamond to demonstrate coherence transfer pathway selection with POPS, and to explore the effects of instantaneous spectral diffusion on P1 center echo decay.

Instantaneous spectral diffusion (ID) can be understood in terms of the dephasing of the observed spins due to flips of neighboring dipole-coupled electron spins, which are caused by the applied microwave pulses. Spin flips which occur during the second pulse produce changes in the local magnetic field seen by observed spins which are not refocused by the Hahn echo. ID leads to spin echo dephasing with a rate $1/T_{ID}$, modifying the phase memory time T_m, the experimentally measured echo decay time constant, according to $1/T_m = 1/T_{ID} + 1/T_2$.[73] T_{ID} depends on the P1 center concentration C_N, and on the refocusing pulse tip angle θ according to[74]

$$\frac{1}{T_{ID}} = C_N \frac{\pi}{9\sqrt{3}} \frac{\mu_0 g^2 \mu_B^2}{\hbar} \left\langle \sin^2\left(\frac{\theta}{2}\right) \right\rangle \quad (10)$$

where the inversion profile of the refocusing pulse $\left\langle \sin^2\left(\frac{\theta}{2}\right) \right\rangle$ with Rabi frequency $\Omega_R = \gamma B_1$ and length t_p is given by

$$\left\langle \sin^2\left(\frac{\theta}{2}\right) \right\rangle = \int_{-\infty}^{\infty} \frac{{\Omega_R}^2}{\delta^2 + {\Omega_R}^2} \sin^2\left(\frac{t_p}{2}\sqrt{\delta^2 + {\Omega_R}^2}\right) f(\delta) \mathrm{d}\delta \quad (11)$$

where $\delta = \omega - \omega_L$ is the detuning, $f(\delta)$ is the normalized lineshape, and ω_L is the Larmor frequency. When the bandwith of the inversion pulse is small relative to the inhomogeneous EPR linewidth so that $\left\langle \sin^2\left(\frac{\theta}{2}\right) \right\rangle \ll 1$, ID is negligible. When the bandwith of the inversion pulse is not small relative to the inhomogeneous EPR linewidth, T_m becomes tip-angle dependent proportional to the concentration C_N. However, by systematically varying the tip angle, and therefore the inversion profile $\left\langle \sin^2\left(\frac{\theta}{2}\right) \right\rangle$ of the inversion pulse, the electron spin concentration C_N and the true electron spin T_2 can be ascertained.[75]

POPS was used to measure the room temperature phase memory time of P1 centers in diamond as a function of the inversion profile of the second pulse, as show in Fig. 4. Fig. 4a-1 shows the time-domain signal generated by a pair of pulses separated by 350 ns which are on resonance with the central hyperfine peak of the P1 center. The FID from the second pulse and the spin-echo overlap substantially in time, and so distort each other. The FID displays modulations due to partial excitation of the outer two hyperfine peaks, while the echo does not as only the central peak is refocused.

In order to cleanly separate the echo signal from the FID signal so that T_m could be measured, coherence transfer pathway selection was performed by repeating the two-pulse experiment while using POPS to cycle the phase of the first pulse through four steps, generating four time traces. The first pulse was cycled through four phases, nominally $\{\Delta\varphi_i\} = \{0°,90°,180°,270°\}$, and experimentally measured to be $\{\Delta\varphi_i\} = \{0°,79°,179°,252°\}$. Fig. 4a-2–a-4 show the post-processed signals generated from the same four time traces, where the numerical phase shifts were chosen using the least-squares method to select for the FID from the second pulse (Fig. 4a-2), for the echo (Fig. 4a-3), and for the FID from the first pulse (Fig. 4a-4), which has decayed below the detection threshold. Further information about the numerical phase shifts chosen is presented in the ESI.† The inversion profile $\left\langle \sin^2\left(\frac{\theta}{2}\right) \right\rangle$ of the second pulse at full power was calculated from the measured EPR lineshape, using t_p = 18 ns and B_1 = 6.4 Gauss. When using an 18 ns, 2.7 kW inversion pulse, T_m was found to be 350 ± 20 ns (Fig. 4c). When the power, and therefore the tip angle, of the inversion pulse was reduced, the echo amplitude decreased, but T_m was found to increase, consistent with the occurrence of instantaneous spectral diffusion. Fig. 4d shows that with the inversion pulse attenuated to 1% power, the phase memory time was extended to 1100 ± 100 ns, an increase of more than a factor of three. Varying the tip angle of the inversion pulse and

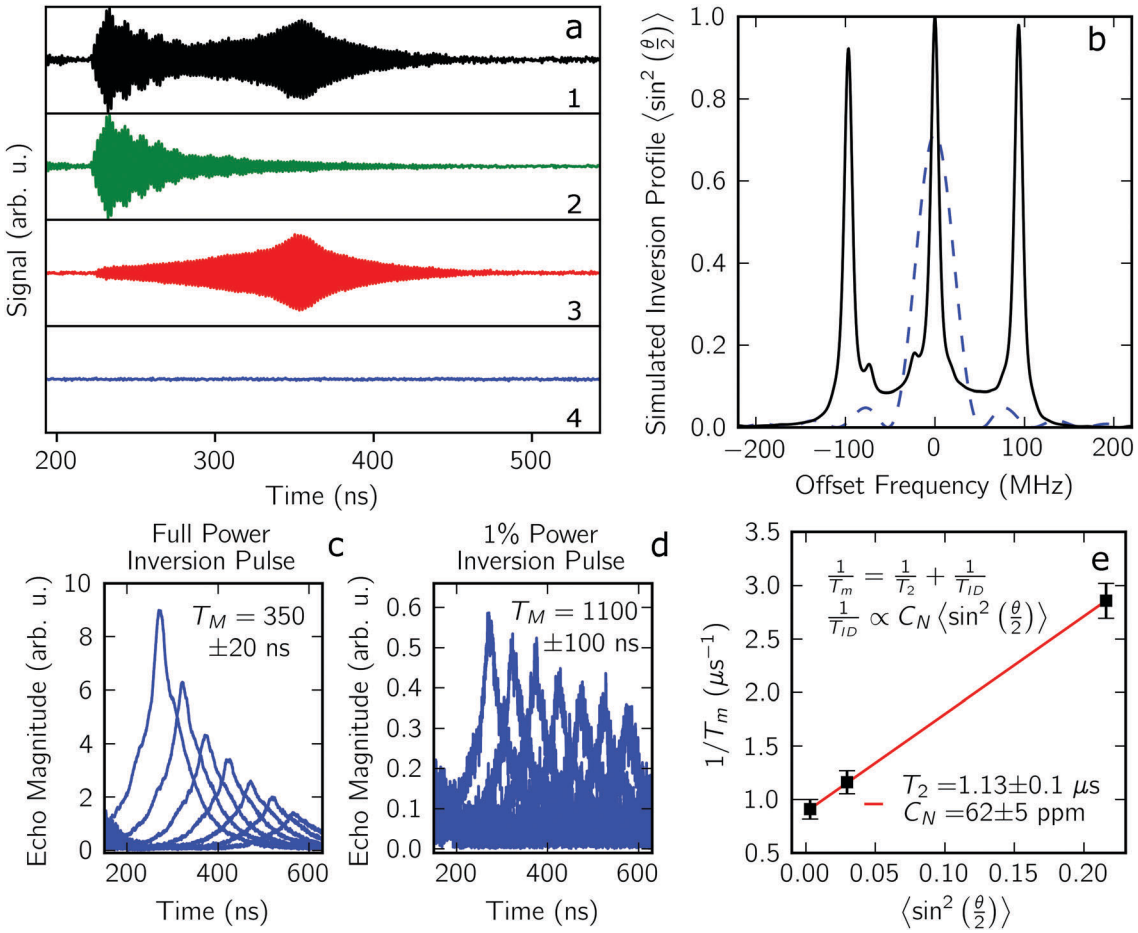

Fig. 4 (a) Signal generated by a two-pulse experiment performed on P1 centers in type 1b diamond, measured on the central line (1) without phase cycling, and with four-step POPS to isolate (2) the FID from the second pulse, (3) the echo generated by the pair of pulses, and (4) the FID from the first pulse. The lengths of pulses one and two were 11 ns and 18 ns, respectively, with an inter-pulse delay of 350 ns. Signal detection begins with the activation of a silicon protection switch, which occurs ~215 ns after the second pulse. The FID generated by the first pulse has decayed below the detection threshold. (b) EPR lineshape of P1 centers in diamond for the sample in question, acquired by field-swept CW EPR at 240 GHz with the field axis converted to frequency. The dotted line shows the simulated inversion profile of the second pulse (eqn (11)), for which B_1 = 6.4 Gauss in the rotating frame. Echo dephasing due to ID is proportional to the degree to which all P1 spins, including those which are not participating in the echo, are inverted by the second pulse. (c) Time domain echo magnitude signals as a function of inter-pulse delay τ, for full power in the second pulse (B_1 = 6.4 Gauss in the rotating frame) and (d) for 1% power in the second pulse (B_1 = 0.64 Gauss in the rotating frame), with the length of the second pulse, and the power and length of the first pulse, all held constant. (e) Inverse phase memory time as a function of the calculated inversion profile of the second pulse $\langle \sin^2(\theta/2) \rangle$, quantifying the effect of instantaneous spectral diffusion on echo dephasing. Extrapolating to $\langle \sin^2(\theta/2) \rangle = 0$, T_2 = 1.13 ± 0.1 μs. From the inverse T_m dependence on B_1, the concentration C_N of P1 centers is estimated to be 62 ± 5 ppm (relative to carbon).

extrapolating to $\left\langle \sin^2\left(\frac{\theta}{2}\right) \right\rangle = 0$, a value of T_2 = 1130 ± 100 ns was calculated (Fig. 4e). T_2 extrapolated in this way is consistent with phase memory time measurements performed on the same sample using 500 ns, low power pulses generated by a 50 mW solid state source, where T_m = 1230 ± 70 ns was measured. From the dependence of $1/T_m$ on $\left\langle \sin^2\left(\frac{\theta}{2}\right) \right\rangle$ in eqn (10), the concentration of P1 centers C_N was estimated to be 62 ± 5 ppm. While the exact P1 center concentration is not known for this sample, this is a reasonable number for type 1b diamond.[11]

3.3 T_1 measurements

Two-pulse saturation-recovery experiments with POPS were used to perform room temperature T_1 measurements on liquid samples of trityl OX063. Shown in Fig. 5, this represents the first measurement of T_1 with FEL-EPR. Fig. 5a shows a free induction decay generated by a 10 ns, 5 kW pulse with γB_1 = 11 Gauss applied to a sample of 3.7 mM trityl OX063 dissolved in D_2O. The Fourier transform of the digitized FID is shown in Fig. 5b, and is well-approximated by a Lorentzian with a FWHM of 9.1 MHz, corresponding to T_2* = 35 ns. This relatively narrow linewidth is fully excited by a 10 ns pulse, so that the sample magnetization can be read out with an FID.

Saturation recovery experiments were performed utilizing the entire long FEL pulse, including the build-up to lasing,[37] as the saturation pulse. Saturation pulses were typically ~1.5–2 μs long, with ~500 W of power. This was achieved by replacing the first "on" switch in the pulse slicer, shown in Fig. 2, with a mirror. The saturation pulse was shut off with the first "off"

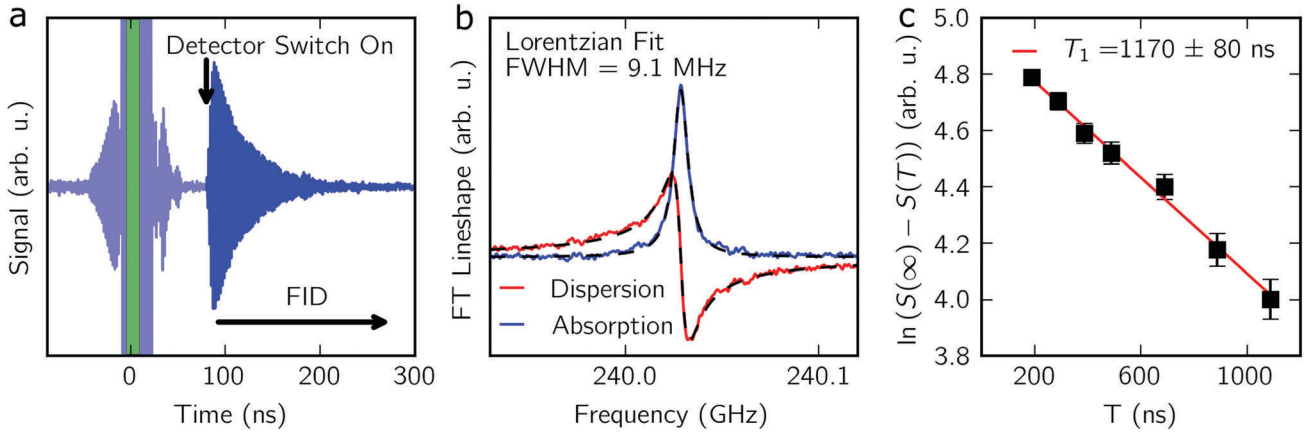

Fig. 5 (a) Time domain FID from 3.7 mM trityl OX063 in D_2O at 291 K, generated by a 10 ns pulse (represented by the green bar) with 15 averages. Arrows mark the time when the detector switch is activated, and indicate the position of the FID. Signal before activation of the detector switch, shown in light blue, is due to incomplete isolation. (b) Fourier transform of the FID from left figure. The complex lineshape is well described by a Lorentzian with a FWHM of 9.1 MHz. (c) Saturation-recovery experiment performed on 3.7 mM trityl OX63 data plotted is natural log of the difference between the integrated FID $S(T)$ as a function if inter-pulse delay T and the integrated FID in the absence of a saturation pulse $S(\infty)$. T_1 = 1170 ± 80 ns is extracted from a linear fit to the data.

switch. After a recovery period T, the magnetization was read out with an FID generated by a 10 ns, 5 kW pulse. Four step POPS was employed to correct for incomplete saturation, and to reduce experimental artifacts. The resulting sequence of FIDs were Fourier transformed, and the integral of the lineshape $V(T)$ used to determine T_1 from the slope of a linear fit to $\ln(V(\infty) - V(T))$, where $V(\infty)$ is the integrated lineshape in the absence of a saturation pulse. T_1 measured by this saturation recovery method was found to be 1170 ± 80 ns. In liquid solutions containing O_2, both T_1 and T_2 relaxation times for both trityl-type radicals and nitroxide radicals are influenced by collisions with paramagnetic O_2,[76,77] are highly dependent on the oxygen partial pressure,[78,79] and are considerably shorter than in deoxygenated aqueous samples.[77,80,81] The value of T_1 reported here is consistent with spin–lattice relaxation times performed at lower fields on oxygenated liquid samples with moderate oxygen concentrations.[76,79]

4 Discussion

Phase cycling enabled by POPS dramatically extends the capabilities of the 240 GHz FEL-EPR spectrometer. First, phase cycling has enabled a ~30 percent reduction in the dead time of the FEL-EPR spectrometer. High power pulses provided by FEL-EPR generate rapid <10 ns spin manipulations, which allow for the study of samples with short relaxation times and broad EPR lines. However, the usefulness of FEL-EPR in studying fast relaxing systems is limited if the experimental dead time restricts the detection of EPR signals to long times. Dead time in FEL-EPR experiments is currently limited by scattered 240 GHz light, and 240 GHz light leaking through imperfect induction-mode isolation. This light, when it reaches the detector, is digitized and distorts or completely masks the EPR signals of interest. While work is underway to minimize scattered and leaked light, this manuscript demonstrates that POPS can efficiently separate the echo generated by a pair of pulses from digitized signals caused by scattered light, reducing the minimum experimental dead time in two pulse spin-echo experiments by ~20 ns, from ~70 ns to ~50 ns. This development dramatically improves the capability of measuring fast-relaxing systems, such as spin-labeled biomolecules at temperatures close to physiological conditions (>200 K) or metal complexes such as gadolinium complexes in the same temperature range.

Second, phase cycling enables one to disentangle signals from a FID and an echo if they overlap in time. Without phase cycling, detection of an echo is limited to experiments with inter-pulse delays significantly longer than the FID lifetime. This restriction is reduced in the same manner as the restriction imposed by scattered light, by using phase cycling to select the echo and suppress the FID. However, since all experimental signals recorded are stored during acquisition, the same set of experiments can be used to select either the echo, suppressing the FID, or to select the FID, suppressing the echo. The former is desired in a two-pulse echo experiment to measure T_2, while the latter is desired in a two-pulse inversion recovery or saturation recovery experiment to measure T_1. If appropriate pulse lengths are chosen, both experiments could be carried out simultaneously in a multiplexed fashion.

Third, phase cycling provides improved sensitivity for all samples by allowing one to probe short inter-pulse delays which maximize the echo amplitude. This improvement in sensitivity, together with the ability to disentangle FID and echo, enabled the identification of instantaneous spectral diffusion in phase memory time measurements of P1 centers in diamond. Beyond the experiments demonstrated here, detection of short-τ echoes is especially crucial for correctly analyzing echo decays with multiple components, or for severely signal-limited samples.

Finally, phase cycling has enabled the first direct measurement of T_1 in a FEL-EPR experiment. A modification of the pulse slicing optics used to generate short pulses for spin manipulations from the long FEL pulse has allowed for the

generation of long saturation pulses which, together with FID detection, was used to conduct saturation-recovery experiments. This new development opens the door to measuring spin–lattice relaxation times of narrow line radicals at room temperature and in liquid samples, a regime of enormous importance for studying biological systems.

5 Conclusion

Robust two- and four-step phase cycling with optomechanical phase shifters (POPS) procedures have been developed for two-pulse FEL-EPR experiments. This method of phase cycling relies on retrospective phase correction, and is generally applicable to any experiment where the source phase is not locked. Phase shifts in POPS are applied quasioptically directly at the detection frequency, with the only requirement being the ability to perform retrospective phase detection and correction.[53] Phase cycling with nearly arbitrary phase shifts was addressed, greatly simplifying the construction of potential future phase cycling experiments. Phase cycling has enabled measurements of the spin–lattice relaxation time T_1 in samples which are amenable to FID detection. POPS as implemented here could also find applications in EPR and DNP experiments employing gyrotrons, provided the gyrotron is phase-stable on the timescale of the desired pulse sequence.

6 Methods and materials

6.1 Phase shifter plate design and fabrication

Phase shifter plates were constructed out of high density polyethylene (HDPE). Slabs of HDPE 9.5 mm thick (McMaster-Carr) were cut into squares and machined to the desired thickness calculated from eqn (3) by carefully sweeping a fly cutter over the surface of the squares, taking off thin layers of HDPE with each pass.

Plate thickness was characterized first by a micrometer, and then by frequency-domain THz spectroscopy using an Agilent PNA N5224A vector network analyzer (VNA) equipped with a set of frequency-extension modules (Virginia Diodes, Inc.). Normal incidence reflectance measurements were performed on each phase shifter plate using a setup described by Bailey *et al.*[82] with the plates backed by air. Reflectance minima occur when the plate thickness h is equal to an integer multiple of half-wavelengths $\lambda/2$,

$$h = \frac{m\lambda}{2n}, \quad n = 1, 2, 3, \ldots \tag{12}$$

where n is the index of refraction.

6.2 EPR samples

$GdCl_3$ samples were prepared by dissolving $GdCl_3{\cdot}6H_2O$ (gadolinium chloride hexahydrate) in a solution of glycerol-d_8/D_2O (0.6 : 0.4 v : v). $GdCl_3{\cdot}6H_2O$ and D_2O were purchased from Sigma Aldrich, and deuterated glycerol was purchased from Cambridge Isotope Labs.

Measurements of P1 centers in diamond were performed on a piece of type 1b diamond with a nitrogen concentration <100 ppm, with dimensions 4.9 mm $\times$ 4.9 mm, and a thickness of 0.5 mm.

OX063 trityl samples were prepared by dissolving OX063 trityl (GE Healthcare) in D_2O. $\sim$0.8 μL of 3.7 mM trityl solution was loaded into a 4 mm long, rectangular cross section capillary made of borosilicate glass (VitroCom VitroTubes) with a sample volume 2 mm wide and 0.1 mm thick. The ends of the capillary were sealed with wax.

6.3 UCSB mm-wave free electron laser

The UCSB free electron lasers operate off of an electron beam accelerated by an electrostatic accelerator to between 2 and 6 MeV. The electron beam is passed through an undulator which causes the electrons to wiggle. This wiggling of the electron beam generates coherent radiation at a frequency which depends on the period of the undulator magnets and on the beam energy. Lasing takes place inside a $\sim$6 m quasioptical resonator, which produces radiation with a longitudinal mode spacing of $\sim$25 MHz. Single-frequency operation is achieved by seeding a single mode of the resonator with a low power injection source (Virginia Diodes, Inc.).[52] Radiation is coupled out of the cavity using a high resistivity silicon wafer. The silicon wafer also acts as a switch[83] which, when activated by a pulse of 532 nm light from a high-powered, frequency-doubled Nd:YAG laser (Big Sky Laser, CFR200) becomes fully reflecting, increasing the power coupled from the resonator by up to a factor of $\sim$8 for a period of 40 ns in a process termed cavity dumping.[37] Typical FEL pulse lengths are 1–5 μs, at a repetition rate of 1 Hz.

THz radiation coupled out of the FEL resonator is transported to the EPR lab through a transport system consisting of quasioptical mirrors and polymethylpentene (TPX) lenses inside a vacuum transport line. At the output of the optical transport system, the power at 240 GHz is typically $\sim$500 W, with the power during the cavity dump pulse enhanced to by a factor of $\sim$8 for 40 ns.[52]

6.4 FEL-EPR spectrometer

The EPR spectrometer used for these experiments operates either with the UCSB mm-FEL, or with a low power solid-state source (VDI) providing 240 GHz radiation. When operating with the FEL, the few μs long high power 240 GHz pulse coupled from the FEL resonator is sent through a set of pulse slicing optics, in order to produce either one or two short pulses with controlled lengths and delays. High resistivity silicon switches are used to turn on and off each pulse. A schematic of the pulse slicer is shown in Fig. 2, which demonstrates how switches are used to slice two pulses from the FEL beam by directing each pulse along a different optical path and then recombining the two pulses before directing them towards the sample. This spatial separation of the pulses allows for the amplitude of each pulse to be independently adjusted, and the phase difference between the two pulses to be controlled. Silicon switches are activated by a pair of high-powered, frequency-doubled Nd:YAG

lasers. The first laser delivers up to 230 mJ at 532 nm in 5 ns (Spectra physics, Quanta Ray GCR-150). The second laser delivers up to 120 mJ at 530 nm in 120 ps (Ekspla, SL312).

The output of the pulse slicer is quasioptically coupled into a 1.25 m long, 18 mm diameter overmoded corrugated waveguide (Thomas Keating Ltd), which tapers down to 5 mm I.D. above the sample position. The waveguide and sample mount are placed in the bore of an actively shielded magnet (Oxford Instruments plc), which is sweepable from 0–12.5 T. The magnet also contains a superconducting sweep coil with a range of $\pm$60 mT about the main coil position. Samples are mounted at the end of the waveguide taper, and are backed by a flat silvered mirror (Thorlabs, Inc.). No resonant cavity was used for these experiments.

The reflected signal is measured in induction mode with a subharmonic Schottky-diode mixer (VDI, WR4.3SHM) driven by a local oscillator. To protect the detector from light leaking though the induction mode quasioptics, a silicon switch is employed which is activated by a 532 nm Nd:YAG laser (Litron Nano-T-250-10) after the FEL pulses have fired. Instrumental dead time is limited to $\sim$70 ns when phase cycling is not employed, primarily due to leakage, standing waves, and scattered light from the pulses. The spectrometer utilizes super-heterodyne detection, whereby the signal is mixed down from 240 GHz to 10 GHz with the subharmonic mixer, then down to 500 MHz which is recorded using a 12.5 GS s^{-1} digitizer (National Instruments PXIe-5186). Post-processing was carried out in home-written LabView and Python scripts.

6.5 Two-pulse Hahn echo experiments with phase cycling

Two-pulse Hahn echo experiments were carried out at $\sim$8.56 T. In a two-pulse Hahn echo experiment, each pulse is controlled by a single Nd:YAG laser synchronized to the firing of the FEL. Each laser produces a high-energy pulse which is split by beam splitters, to activate both a silicon ''on'' switch and two silicon ''off'' switches. The length of each pulse is set by variable-length laser delay lines, while the delay between the pulses is set electronically by controlling the timing of the lasers, using a trio of digital delay generators (one SRS DG645, two SRS DG535's). The second pulse is timed to be within the FEL cavity dump pulse, and therefore has its power boosted relative to the first pulse by $\sim 8\times$.

The phase difference between the two pulses is determined by small differences in the optical path length through which each pulse travels. This phase difference is modified by inserting precision machined dielectric plates in pairs at Brewster's angle into the path of the first pulse. For the experiments presented here, the phase shifter plates were inserted and removed manually. Manual insertion and removal of the plates took several seconds. For future experiments, we are working to automate this process to save time.

Experiments on $GdCl_3$ were performed at cryogenic temperatures utilizing a flow cryostat (Janis Research Co.). 14 μL of sample was placed in a cylindrical Teflon sample cup with a $\sim$3.5 mm inner diameter and a height of $\sim$5 mm, backed by a mirror, and placed at the end of the waveguide taper. Cooling was achieved with cold nitrogen gas boiled off of a liquid nitrogen reservoir. Pulse lengths were 11 ns for pulse one, and 7 ns for pulse two.

Experiments on P1 centers in diamond were performed at room temperature. The diamond sample was backed with a mirror and placed at the end of the waveguide taper. Pulse lengths were 11 ns for pulse one, and 18 ns for pulse two. Attenuation of the second pulse for quantification of instantaneous spectral diffusion was achieved by placing calibrated THz attenuators (Tydex) in the arm of the pulse slicer generating the second pulse.

6.6 Saturation recovery experiments with phase cycling to measure T_1

Saturation pulses were generated by replacing the ''on'' switch for the first pulse with a mirror allowing for a saturation pulse of 1.5–2 μs long and was turned off with silicon switches. After an electronically controlled delay, the sample magnetization was read out with a free induction decay (FID) using a 10 ns pulse, making use of the high-power FEL cavity dump pulse. Experiments were performed at room temperature at 8.56 T on aqueous solutions of trityl OX063. A rectangular cross section capillary containing $\sim$0.8 μL of trityl solution was placed on a silicon substrate backed by a mirror. The sample was placed at the end of the waveguide taper.

6.7 Diamond P1 center lineshape and relaxation time measurements

EPR lineshape and low-power relaxation measurements were carried out on the type 1b diamond sample under the same experimental conditions, and in the same spectrometer, using a 50 mW solid-state 240 GHz source (Virginia Diodes, Inc.), which is the same source as used for injection locking for FEL-EPR.[52] Detection is the same, except that the signal is mixed down to DC rather than to 500 MHz for digitization. The P1 center CW EPR lineshape was measured with the superconducting sweep coil, with the 240 GHz source attenuated to $\sim$3 mW. Measurements of T_m with the low-power source were conducted using 50 mW of source power, with pulse lengths of 500 ns. Decay curves were fit to a single exponential.

6.8 Retrospective phase correction and phase cycling calculations

Retrospective phase correction[53] was implemented in LabView, offering real-time coherent signal averaging. Calculations of the correct set of receiver phases were carried out in python, once a set of phase cycled data had been acquired.

The least-squares method of assigning numerical receiver phases was carried out using a Levenberg–Marquardt algorithm, implemented in python using the curve_fit function from the scipy library.

Conflicts of interest

There are no conflicts to declare.

Acknowledgements

CBW, SA, JAC, SH, and MSS gratefully acknowledge support from the National Science Foundation through Molecular and Cellular Biology grants NSF-MCB 1244651 and NSF-MCB 1617025; SJG gratefully acknowledges support from the DFG through grant DFG SPP 1601 New Frontiers in Sensitivity for EPR Spectroscopy: From Biological Cells to Nano Matherials (Project GL 203/7-2).

References

1 S. Schlick, *Advanced ESR methods in polymer research*, Wiley-Interscience, Hoboken, N.J., 2006.
2 A. Savitsky and K. Möbius, *Photosynth. Res.*, 2009, **102**, 311–333.
3 S. K. Misra, *Multifrequency electron paramagnetic resonance theory and applications*, Wiley-VCH, John Wiley [distributor], Weinheim, Chichester, 2011.
4 D. Kurad, G. Jeschke and D. Marsh, *Biophys. J.*, 2003, **85**, 1025–1033.
5 Z. Zhang, M. R. Fleissner, D. S. Tipikin, Z. Liang, J. K. Moscicki, K. A. Earle, W. L. Hubbell and J. H. Freed, *J. Phys. Chem. B*, 2010, **114**, 5503–5521.
6 L. Mainali, J. S. Hyde and W. K. Subczynski, *J. Magn. Reson.*, 2013, **226**, 35–44.
7 V. P. Denysenkov, D. Biglino, W. Lubitz, T. F. Prisner and M. Bennati, *Angew. Chem., Int. Ed.*, 2008, **47**, 1224–1227.
8 S. Stoll, A. Gunn, M. Brynda, W. Sughrue, A. C. Kohler, A. Ozarowski, A. J. Fisher, J. C. Lagarias and R. D. Britt, *J. Am. Chem. Soc.*, 2009, **131**, 1986–1995.
9 S. Takahashi, R. Hanson, J. van Tol, M. S. Sherwin and D. D. Awschalom, *Phys. Rev. Lett.*, 2008, **101**, 047601.
10 C. Abeywardana, V. Stepanov, F. H. Cho and S. Takahashi, *J. Appl. Phys.*, 2016, **120**, 123907.
11 V. Stepanov and S. Takahashi, *Phys. Rev. B*, 2016, **94**, 024421.
12 M. Pannier, S. Veit, A. Godt, G. Jeschke and H. Spiess, *J. Magn. Reson.*, 2000, **142**, 331–340.
13 L. Kulik, S. Dzuba, I. Grigoryev and Y. Tsvetkov, *Chem. Phys. Lett.*, 2001, **343**, 315–324.
14 B. E. Bode, J. Plackmeyer, M. Bolte, T. F. Prisner and O. Schiemann, *J. Organomet. Chem.*, 2009, **694**, 1172–1179.
15 B. E. Bode, J. Plackmeyer, T. F. Prisner and O. Schiemann, *J. Phys. Chem. A*, 2008, **112**, 5064–5073.
16 A. Giannoulis, C. L. Motion, M. Oranges, M. Buhl, G. M. Smith and B. E. Bode, *Phys. Chem. Chem. Phys.*, 2018, **20**, 2151–2154.
17 A. Potapov, H. Yagi, T. Huber, S. Jergic, N. E. Dixon, G. Otting and D. Goldfarb, *J. Am. Chem. Soc.*, 2010, **132**, 9040–9048.
18 D. Edwards, T. Huber, S. Hussain, K. Stone, M. Kinnebrew, I. Kaminker, E. Matalon, M. Sherwin, D. Goldfarb and S. Han, *Structure*, 2014, **22**, 1677–1686.
19 A. Martorana, G. Bellapadrona, A. Feintuch, E. Di Gregorio, S. Aime and D. Goldfarb, *J. Am. Chem. Soc.*, 2014, **136**, 13458–13465.
20 M. Qi, A. Groß, G. Jeschke, A. Godt and M. Drescher, *J. Am. Chem. Soc.*, 2014, **136**, 15366–15378.
21 D. Banerjee, H. Yagi, T. Huber, G. Otting and D. Goldfarb, *J. Phys. Lett.*, 2012, **3**, 157–160.
22 H. Y. V. Ching, F. C. Mascali, H. C. Bertrand, E. M. Bruch, P. Demay-Drouhard, R. M. Rasia, C. Policar, L. C. Tabares and S. Un, *J. Phys. Lett.*, 2016, **7**, 1072–1076.
23 D. T. Edwards, S. Takahashi, M. S. Sherwin and S. Han, *J. Magn. Reson.*, 2012, **223**, 198–206.
24 G. M. Smith, J. C. G. Lesurf, R. H. Mitchell and P. C. Riedi, *Rev. Sci. Instrum.*, 1998, **69**, 3924.
25 M. M. Hertel, V. P. Denysenkov, M. Bennati and T. F. Prisner, *Magn. Reson. Chem.*, 2005, **43**, S248–S255.
26 V. P. Denysenkov, T. F. Prisner, J. Stubbe and M. Bennati, *Appl. Magn. Reson.*, 2005, **29**, 375–384.
27 G. W. Morley, L.-C. Brunel and J. van Tol, *Rev. Sci. Instrum.*, 2008, **79**, 064703.
28 A. A. Smith, B. Corzilius, J. A. Bryant, R. DeRocher, P. P. Woskov, R. J. Temkin and R. G. Griffin, *J. Magn. Reson.*, 2012, **223**, 170–179.
29 I. Tkach, K. Halbmair, C. Höbartner and M. Bennati, *Appl. Magn. Reson.*, 2014, **45**, 969–979.
30 F. H. Cho, V. Stepanov, C. Abeywardana and S. Takahashi, *Methods in Enzymology*, 2015, vol. 563, pp. 95–118.
31 W. Hofbauer, K. A. Earle, C. R. Dunnam, J. K. Moscicki and J. H. Freed, *Rev. Sci. Instrum.*, 2004, **75**, 1194–1208.
32 D. Goldfarb, Y. Lipkin, A. Potapov, Y. Gorodetsky, B. Epel, A. M. Raitsimring, M. Radoul and I. Kaminker, *J. Magn. Reson.*, 2008, **194**, 8–15.
33 P. A. S. Cruickshank, D. R. Bolton, D. A. Robertson, R. I. Hunter, R. J. Wylde and G. M. Smith, *Rev. Sci. Instrum.*, 2009, **80**, 103102.
34 E. A. Nanni, S. M. Lewis, M. A. Shapiro, R. G. Griffin and R. J. Temkin, *Phys. Rev. Lett.*, 2013, **111**, 235101.
35 E. A. Nanni, S. Jawla, S. M. Lewis, M. A. Shapiro and R. J. Temkin, *Appl. Phys. Lett.*, 2017, **111**, 233504.
36 G. Ramian, *Nucl. Instrum. Methods Phys. Res., Sect. A*, 1992, **318**, 225–229.
37 S. Takahashi, G. Ramian and M. S. Sherwin, *Appl. Phys. Lett.*, 2009, **95**, 234102.
38 K. Sakamoto, A. Kasugai, K. Takahashi, R. Minami, N. Kobayashi and K. Kajiwara, *Nat. Phys.*, 2007, **3**, 411–414.
39 S. Alberti, F. Braunmueller, T. M. Tran, J. Genoud, J.-P. Hogge, M. Q. Tran and J.-P. Ansermet, *Phys. Rev. Lett.*, 2013, **111**, 205101.
40 L. R. Becerra, G. J. Gerfen, R. J. Temkin, D. J. Singel and R. G. Griffin, *Phys. Rev. Lett.*, 1993, **71**, 3561–3564.
41 C. Song, K.-N. Hu, C.-G. Joo, T. M. Swager and R. G. Griffin, *J. Am. Chem. Soc.*, 2006, **128**, 11385–11390.
42 A. B. Barnes, E. A. Nanni, J. Herzfeld, R. G. Griffin and R. J. Temkin, *J. Magn. Reson.*, 2012, **221**, 147–153.
43 E. P. Saliba, E. L. Sesti, F. J. Scott, B. J. Albert, E. J. Choi, N. Alaniva, C. Gao and A. B. Barnes, *J. Am. Chem. Soc.*, 2017, **139**, 6310–6313.
44 S. Takahashi, L.-C. Brunel, D. T. Edwards, J. van Tol, G. Ramian, S. Han and M. S. Sherwin, *Nature*, 2012, **489**, 409–413.
45 F. A. Hegmann and M. S. Sherwin, *Generation Of Picosecond Far-Infrared Pulses Using Laser-Activated Semiconductor Reflection Switches*, 1996, pp. 90–106.

46 S. Mitsudo, T. Furuya, Y. Shimoyama, T. Fujita, Y. Tatematsu, T. Idehara and T. Saito, 2009 34th International Conference on Infrared, Millimeter, and Terahertz Waves, 2009, pp. 1–2.
47 G. Bodenhausen, H. Kogler and R. Ernst, *J. Magn. Reson. (1969–1992)*, 1984, **58**, 370–388.
48 C. Gemperle, G. Aebli, A. Schweiger and R. Ernst, *J. Magn. Reson. (1969–1992)*, 1990, **88**, 241–256.
49 A. Schweiger and G. Jeschke, *Principles of pulse electron paramagnetic resonance*, Oxford University Press, Oxford, UK, New York, 2001.
50 T. Kaufmann, T. J. Keller, J. M. Franck, R. P. Barnes, S. J. Glaser, J. M. Martinis and S. Han, *J. Magn. Reson.*, 2013, **235**, 95–108.
51 I. Kaminker, R. Barnes and S. Han, *J. Magn. Reson.*, 2017, **279**, 81–90.
52 S. Takahashi, G. Ramian, M. S. Sherwin, L.-C. Brunel and J. van Tol, *Appl. Phys. Lett.*, 2007, **91**, 174102.
53 D. T. Edwards, Y. Zhang, S. J. Glaser, S. Han and M. S. Sherwin, *Phys. Chem. Chem. Phys.*, 2013, **15**, 5707–5719.
54 N. Ivchenko, C. E. Hughes and M. H. Levitt, *J. Magn. Reson.*, 2003, **160**, 52–58.
55 A. D. Bain, *J. Magn. Reson. (1969–1992)*, 1984, **56**, 418–427.
56 R. R. Ernst, *Principles of nuclear magnetic resonance in one and two dimensions*, Clarendon Press, Oxford University Press, Oxford [Oxfordshire], New York, 1987.
57 J. Keeler, *Understanding NMR spectroscopy*, Wiley, Chichester, England, Hoboken, NJ, 2005.
58 M. H. Levitt, *Spin dynamics: basics of nuclear magnetic resonance*, John Wiley & Sons, Chichester, England, Hoboken, NJ, 2nd edn, 2008.
59 J. Birch, J. Dromey and J. Lesurf, *Infrared Phys.*, 1981, **21**, 225–228.
60 R. Piesiewicz, C. Jansen, S. Wietzke, D. Mittleman, M. Koch and T. Kürner, *Int. J. Infrared Millimeter Waves*, 2007, **28**, 363–371.
61 D. Reichert and G. Hempel, *Concepts Magn. Reson.*, 2002, **14**, 130–139.
62 D. Goldfarb, *Phys. Chem. Chem. Phys.*, 2014, **16**, 9685–9699.
63 A. M. Raitsimring, C. Gunanathan, A. Potapov, I. Efremenko, J. M. L. Martin, D. Milstein and D. Goldfarb, *J. Am. Chem. Soc.*, 2007, **129**, 14138–14139.
64 D. T. Edwards, Z. Ma, T. J. Meade, D. Goldfarb, S. Han and M. S. Sherwin, *Phys. Chem. Chem. Phys.*, 2013, **15**, 11313–11326.
65 J. A. Clayton, M. Qi, A. Godt, D. Goldfarb, S. Han and M. S. Sherwin, *Phys. Chem. Chem. Phys.*, 2017, **19**, 5127–5136.
66 S. Razzaghi, M. Qi, A. I. Nalepa, A. Godt, G. Jeschke, A. Savitsky and M. Yulikov, *J. Phys. Lett.*, 2014, **5**, 3970–3975.
67 A. Raitsimring, A. Dalaloyan, A. Collauto, A. Feintuch, T. Meade and D. Goldfarb, *J. Magn. Reson.*, 2014, **248**, 71–80.
68 J. A. van Wyk, E. C. Reynhardt, G. L. High and I. Kiflawi, *J. Phys. D: Appl. Phys.*, 1997, **30**, 1790.
69 Z.-H. Wang and S. Takahashi, *Phys. Rev. B: Condens. Matter Mater. Phys.*, 2013, **87**, 115122.
70 A. Jarmola, V. M. Acosta, K. Jensen, S. Chemerisov and D. Budker, *Phys. Rev. Lett.*, 2012, **108**, 197601.
71 T. Wolf, P. Neumann, K. Nakamura, H. Sumiya, T. Ohshima, J. Isoya and J. Wrachtrup, *Phys. Rev. X*, 2015, **5**, 041001.
72 C. Grezes, B. Julsgaard, Y. Kubo, W. L. Ma, M. Stern, A. Bienfait, K. Nakamura, J. Isoya, S. Onoda, T. Ohshima, V. Jacques, D. Vion, D. Esteve, R. B. Liu, K. Mølmer and P. Bertet, *Phys. Rev. A: At., Mol., Opt. Phys.*, 2015, **92**, 020301.
73 J. R. Klauder and P. W. Anderson, *Phys. Rev.*, 1962, **125**, 912–932.
74 K. Salikhov, S. Dzuba and A. Raitsimring, *J. Magn. Reson. (1969–1992)*, 1981, **42**, 255–276.
75 A. M. Tyryshkin, S. Tojo, J. J. L. Morton, H. Riemann, N. V. Abrosimov, P. Becker, H.-J. Pohl, T. Schenkel, M. L. W. Thewalt, K. M. Itoh and S. A. Lyon, *Nat. Mater.*, 2012, **11**, 143–147.
76 C. A. Popp and J. S. Hyde, *J. Magn. Reson. (1969–1992)*, 1981, **43**, 249–258.
77 R. Owenius, G. R. Eaton and S. S. Eaton, *J. Magn. Reson.*, 2005, **172**, 168–175.
78 W. K. Subczynski and J. S. Hyde, *Biochim. Biophys. Acta, Biomembr.*, 1981, **643**, 283–291.
79 B. Epel, M. K. Bowman, C. Mailer and H. J. Halpern, *Magn. Reson. Med.*, 2014, **72**, 362–368.
80 W. K. Subczynski, L. Mainali, T. G. Camenisch, W. Froncisz and J. S. Hyde, *J. Magn. Reson.*, 2011, **209**, 142–148.
81 A. A. Kuzhelev, D. V. Trukhin, O. A. Krumkacheva, R. K. Strizhakov, O. Y. Rogozhnikova, T. I. Troitskaya, M. V. Fedin, V. M. Tormyshev and E. G. Bagryanskaya, *J. Phys. Chem. B*, 2015, **119**, 13630–13640.
82 M. L. P. Bailey, A. T. Pierce, A. J. Simon, D. T. Edwards, G. J. Ramian, N. I. Agladze and M. S. Sherwin, *IEEE Trans. Terahertz Sci. Technol.*, 2015, **5**, 961–966.
83 M. F. Doty, B. E. Cole, B. T. King and M. S. Sherwin, *Rev. Sci. Instrum.*, 2004, **75**, 2921–2925.